Monthly Notices of the ROYAL ASTRONOMICAL SOCIETY

MNRAS **475,** 3746–3763 (2018)
Advance Access publication 2018 January 4

doi:10.1093/mnras/stx3351

Variations in the 6.2 μm emission profile in starburst-dominated galaxies: a signature of polycyclic aromatic nitrogen heterocycles (PANHs)?

Carla M. Canelo,[1★] Amâncio C. S. Friaça,[1] Dinalva A. Sales,[2] Miriani G. Pastoriza[3] and Daniel Ruschel-Dutra[4]

[1]*Departamento de Astronomia, Instituto de Astronomia, Geofísica e Ciências Atmosféricas, Universidade de São Paulo, 05508-090 São Paulo, Brazil*
[2]*Instituto de Matemática, Estatística e Física, Universidade Federal do Rio Grande, 96201-900 Rio Grande do Sul, Brazil*
[3]*Instituto de Física, Universidade Federal do Rio Grande do Sul, 91501-970 Rio Grande do Sul, Brazil*
[4]*Centro de Física e Matemática, Universidade Federal de Santa Catarina, 88040-900 Santa Catarina, Brazil*

Accepted 2017 December 27. Received 2017 December 22; in original form 2017 June 14

ABSTRACT

Analyses of the polycyclic aromatic hydrocarbon (PAH) feature profiles, especially the 6.2 μm feature, could indicate the presence of nitrogen incorporated in their aromatic rings. In this work, 155 predominantly starburst-dominated galaxies (including H II regions and Seyferts, for example), extracted from the *Spitzer*/Infrared Spectrograph ATLAS project, have their 6.2 μm profiles fitted allowing their separation into the Peeters' A, B, and C classes. 67 per cent of these galaxies were classified as class A, 31 per cent were as class B, and 2 per cent as class C. Currently, class A sources, corresponding to a central wavelength near 6.22 μm, seem only to be explained by polycyclic aromatic nitrogen heterocycles (PANHs), whereas class B may represent a mix between PAHs and PANHs emissions or different PANH structures or ionization states. Therefore, these spectra suggest a significant presence of PANHs in the interstellar medium (ISM) of these galaxies that could be related to their starburst-dominated emission. These results also suggest that PANHs constitute another reservoir of nitrogen in the Universe, in addition to the nitrogen in the gas phase and ices of the ISM.

Key words: astrobiology – astrochemistry – ISM: molecules – galaxies: ISM – infrared: galaxies.

1 INTRODUCTION

A considerable fraction of the carbon in the interstellar medium (ISM), 20 per cent or more, is in the form of polycyclic aromatic hydrocarbons (PAHs; Joblin, Leger & Martin 1992). In addition, the mid-infrared (MIR) emission from many objects is dominated by bands of a molecular class, which includes PAHs, sometimes referred to the Aromatic Infra-red Bands (AIBs; Joblin et al. 1992). All other classes of organics and inorganics represent only a tiny fraction of the emitting material that contributes to the AIBs (Allamandola, Hudgins & Sandford 1999). Up to 50 per cent of the luminosity emitted in the MIR can be due to PAHs, with the most prominent bands emitting at 3.3, 6.2, 7.7, 8.6, 11.3, and 12.7 μm (Li 2004). Their high luminosity allows them to be observed in high-redshift objects, where they may dominate the IR spectrum range (Papovich et al. 2006; Teplitz et al. 2007). Recently, the largest redshift in which PAH bands were detected was for the Cosmic Eye Galaxy with z =3.074, a Lyman Break Galaxy with strong gravitational lens (Siana et al. 2009). Years later, the 6.2 μm band was observed in the submillimetre galaxy GN20, with a redshift of $z = 4.055$ (Riechers et al. 2014).

Because of their stable molecular structure, PAHs are the dominant molecular organic material in space (Ehrenfreund et al. 2006) and, together with other aromatic macromolecules, they are the most abundant class of molecular species that must have been transported to the planets by comets, meteorites, and interplanetary dust deposition (Ehrenfreund et al. 2002). Produced in other parts of the Solar system or Galaxy, they have been delivered almost intact to planets such as Earth and Mars. They could also have undergone a stage of production of nitrogen heterocyclic molecules which, along with PAHs, are of a great astrobiological interest. In addition, in the PAH World model for the origins of life, they played a key role in the stages preceding the RNA World (Ehrenfreund et al. 2006), not only on Earth but in other astrophysical environments as well.

When a PAH incorporates nitrogen in place of a carbon atom, it is called a polycyclic aromatic nitrogen heterocycle (PANH). It has been suggested that a significant fraction of the nitrogen in the ISM is depleted into PANHs (Hudgins et al. 2005). Peeters et al. (2002) considered the 6–9 μm spectral range of several astrophysical objects and studied the presence of profile variations among the PAH bands. They found that their sample could be separated into

★ E-mail: camcanelo@gmail.com

three different classes – A, B, and C – depending on the peak positions of the bands. Later, van Diedenhoven et al. (2004) extended the approach for the 3.3 and 11.2 μm bands and revealed a correlation between the classification of the PAH bands and their profiles.

In general, an A classification in the 6–9 μm region also implies an $A_{3.3}$ and $A_{11.2}$, but $B_{3.3}$ and $B_{11.2}$ do not necessarily correlate with each other or with $B_{6–9}$ and $C_{6–9}$. Normally, the profile A peaks at 6.2 μm while profiles B and C peak at longer wavelengths. The classes A and B differ largely in the relative strength of subcomponents at 7.6 and 7.8 μm, which seem to have shifted to 8.2 μm for class C (Tielens 2008). Also, the classes are linked to the type of source. Class A sources are associated with interstellar material illuminated by a star, including H II regions, reflection nebulae, and the general ISM of the Milky Way and other galaxies. Class B objects are associated with circumstellar material and include planetary nebula, a variety of post-AGB objects and Herbig AeBe stars. Class C sources are limited to a few extreme carbon-rich post-AGB objects.

Thus, analyses of PAH feature profiles, especially the 6.2 μm band, could indicate the presence of nitrogen incorporated into the rings. The class A 6.2 μm band corresponds to a central wavelength at 6.22 μm and has only been well reproduced by carbon replaced by nitrogen into the aromatic rings (Hudgins et al. 2005). These PAH features are prominent in star-forming systems, reduced and modified in high-intensity starbursts and, eventually, disappear in active galactic nuclei (AGNs) systems (Yan et al. 2007). The spectral continuum shape of starburst spectra is dominated by strong emission features from PAHs (Genzel & Cesarsky 2000) and the 5–8 μm spectral range of starburst galaxies is not only extremely rich in atomic and molecular emission and absorption features but is also dominated by emission from the 6.2 μm PAH feature and the blue wing of the 7.7 μm PAH complex (Brandl et al. 2006). In fact, the emission and absorption features of dust grains predominate the MIR spectra of starburst galaxies and most ULIRGs (ultraluminous infrared galaxies; Yan et al. 2005).

Identification of the feature classes can show if PANHs may be present in the spectrum of the sources and account for this PAH band of the MIR emission. With this in mind, we here analysed and classified the 6.2 μm feature of 206 galaxies observed with *Spitzer* according to the Peeters' classes, searching for the PANH contribution to this PAH band. This paper is structured as follows: Section 2 explains the selection of our sample and Section 3 describes the data analysis performed in the spectroscopic data. Results are discussed in Section 4 and Section 5 presents the summary and conclusion.

2 DATA SELECTION

The *Spitzer*/Infrared Spectrograph (IRS) ATLAS project (Hernán-Caballero & Hatziminaoglou 2011) possesses around 750 reduced spectra of several types of extragalactic objects, such as Seyfert, radiogalaxies, and submillimetre galaxies. They were observed in low and high resolution by the IRS (Houck et al. 2004) of the *Spitzer* Space Telescope (Werner et al. 2004) and their reduced spectra were extracted from Post-script figures uploaded to the arxiv.org pre-print service by their authors. The ATLAS project also offers the best redshift values of the sources found in the literature and checked with NED (NASA Extragalactic Database). The data are not at the rest wavelength and, for this correction, we used values published by the authors (see Table A1). However, in the case of high redshifts, the values could have been obtained only through PAH bands themselves or through the IRS spectrum, with no other accurate measure. According to Weedman et al. (2006), the uncertainties for spectroscopic redshifts greater than 1 from IRS spectrum are typically ±0.2. These sources are indicated in the table. This situation may interfere with the rest wavelengths of the spectra and compromise the original peak position of the features. For this reason, these cases must take into account a possible extra shift in the 6.2 μm central wavelength for the analysis.

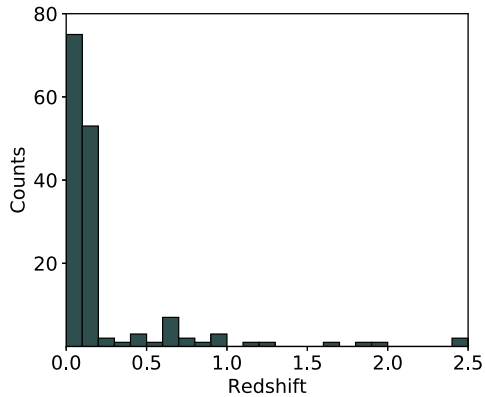

Figure 1. Histogram of the 155 redshifts of our galaxy's sample.

The spectra may have an inferior quality if compared to the fully and properly reduced spectra because, in some cases, the flux uncertainties are missing or the spectra are smoothed, for instance. The accuracy with which the original wavelength and flux values are recovered is limited by the resolution of the Post-script figure, once they were transformed from the Post-script coordinates (sets of points representing the spectra in the figures; Hernán-Caballero & Hatziminaoglou 2011). Nevertheless, according to the authors, the resulting introduced uncertainty to the wavelength calibration is an order of magnitude smaller than the spectral resolution ($R \sim 100$) in the low-resolution module of IRS. Therefore, its impact is negligible and statistical analysis of the sample is little, if at all, affected (Hernán-Caballero & Hatziminaoglou 2011).

For a better understanding of the PANH distribution in the Universe, starburst galaxies are the best targets since they carry different burst of young stellar population and, consequently, present strong PAH emission in the MIR spectral wavelengths. We therefore selected objects from the ATLAS MIR starburst-dominated galaxies (MIR_SB sample), which is composed of 257 sources previously classified as starburst-dominated by Hernán-Caballero & Hatziminaoglou (2011). The limit set between AGN- and starburst-dominated sources was based on the fraction of a PDR (photodissociation region) component at $r_{PDR} = 0.15$, corresponding to equivalent widths (EW) of $EW_{6.2} = 0.2$ μm or $EW_{11.3} = 0.2$ μm as an alternative boundary.

From their subsample, 219 objects have a wavelength coverage that includes the 6.2 μm PAH band. However, some galaxies do not have enough data points for a trustworthy fit or the profiles were peculiar and were not used in this work. We also included two other ULIRGs observed by Yan et al. (2007) due to their strong PAH features. Table A1 presents information of our sample that is composed by 155 galaxies. The distribution of the redshifts can be seen in Fig. 1 .

3 DATA ANALYSIS

Before the 6.2 μm feature profile was fitted, the spectral contributions of the silicate absorption and line emissions were subtracted

from the spectra using PAHFIT (Smith et al. 2007). This IDL[1] script was created to decompose low-resolution IRS spectra into dust features, stellar and thermal dust continuum, silicate absorption, and ionic and molecular line emission. Although PAHFIT also recovers PAH features, the central wavelengths of the bands are fixed in the code. This lack of flexibility prevents the account of the peak position variations and the fits of PAH bands obtained with this tool were disregarded in this work.

The continuum of the galaxies was fitted with a spline with anchor points at roughly 5.0, 5.4, 5.5, 5.8, 6.6, 7.0, 8.2, 9.0, 9.3, 9.9, 10.2, 10.5, 10.7, 11.7, 12.1, 13.1, 13.9, 14.7, and 15.0 μm according to the method utilized in Peeters et al. (2017). The inclusion of each point depended on the presence of the PAH plateaus (at 5–10 and 10–15 μm) and molecular bands (at 10.68 μm, for example). The spline decomposition was chosen because it allows us to isolate the 6.2 μm band.

As already discussed in Peeters et al. (2017), the overall conclusions on PAH intensity correlations for a large sample of objects are independent of the chosen decomposition approach (e.g. Smith et al. 2007; Galliano et al. 2008). However, we analysed 20 galaxies of our sample – 10 with strong PAH plateaus and 10 with none or weak plateaus – in order to perceive the stability of our 6.2 μm fitting according to the continuum decomposition obtained with spline and with PAHFIT. These galaxies have their 6.2 μm profile fitted (as it will be discussed in the next section) and the results revealed that the band intensities and the full width at half-maximum (FWHM) showed greater discrepancies but the central wavelengths had no significant changes. Therefore, we can conclude that the presence of plateaus did not influence the results. As our work focuses on peak position of the profile, the chosen continuum decomposition applied does not interfere in the final analysis. A discussion of this comparison can be found in the Appendix B. Two examples of these decompositions can be seen in Figs 2 and 3, with and without PAH plateaus, respectively.

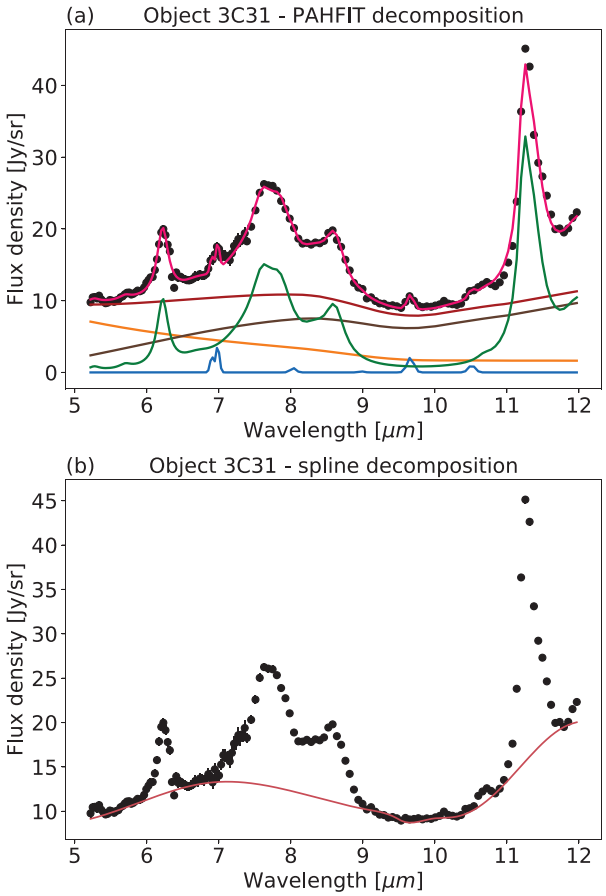

Figure 2. Comparison between the spectral decomposition with PAHFIT and with spline continuum for an object with the PAH plateaus. (a) Result of the PAHFIT decomposition of the 3C31 spectrum. The data points are represented by the dots with the vertical error bars as uncertainties. The pink line corresponds to the best-fitting model, the green line is the dust (AIB, PAH) contribution, and blue one is the ionic and molecular lines contribution. The red line represents the total continuum contribution, and the brown and orange lines correspond to its individual thermal and stellar components, respectively. (b) The red line represents the spline decomposition of the continuum. The data points are represented by the dots with the vertical error bars as uncertainties.

3.1 The 6.2 μm feature profile

The differences among the 6.2 μm PAH profiles in such astrophysical environments have been attributed, for example, to the local physical conditions and of the PAH molecules' size, charge, geometry, and heterogeneity (e.g. Draine & Li 2001, 2007; Smith et al. 2007; Sales et al. 2012). The CC vibration modes of the 5–9 μm wavelengths produce profiles (and their peak positions) highly variable, even in relatively low-resolution data (Tielens 2008). On the other hand, CH modes vary less and the variation may not be necessarily connected to the others (van Diedenhoven et al. 2004; Tielens 2008; Candian & Sarre 2015).

According to Hudgins & Allamandola (1999), PAHs with roughly 20 carbon atoms already contribute to the 6.2 μm emission and the spacing among the PAH bands increases with molecular size. In general, for this band, objects grouped in class A have an asymmetric profile composed of a sharp blue rise and a red tail with central wavelength varying up to 6.23 μm (Peeters et al. 2002). In classes B and C, this asymmetry decreases and, for the C, the peak position is greater than 6.29 μm. As already discussed, Hudgins et al. (2005) considered the blueshift of this band (peak positions $\leq$6.22 μm) which characterizes a class A object. The increase of PAH size, the substitution of carbon atoms by silicon or oxygen, the metal ion complexation (Fe^{+}, Mg^{+}, and Mg^{2+}), and the molecular symmetry variation were not able to reproduce the observed position of this interstellar band while simultaneously satisfying the astrophysical implications (for instance, the cosmic abundance of the chemically reactive elements). Apparently, of the possible substitutions they consider, nitrogen incorporated into the inner part of the rings is the only solution capable of reproducing the observed profile. The authors also estimated that a lower limit of 1–2 per cent of the cosmic nitrogen is retained in the PAH molecules located in the ISM (e.g. Hudgins, Bauschlicher & Allamandola 2005; Boersma, Bregman & Allamandola 2013; Boersma et al. 2014).

To accomplish this study of the 6.2 μm PAH profile of starburst galaxies, we constructed a PYTHON-based script to estimate its central wavelength through the optimization algorithms from the submodule *scipy.optmize.curve_fit* (hereafter *curve_fit*). The data were fitted by a Gaussian profile (equation 1). The uncertainties were also derived using this tool with least-squares minimization and we used normalized root mean square (rms) deviation to evaluate the quality of the fit (equation 2). The initial guesses selected

[1] Interactive Data Language, available at http://ittvis.com/idl

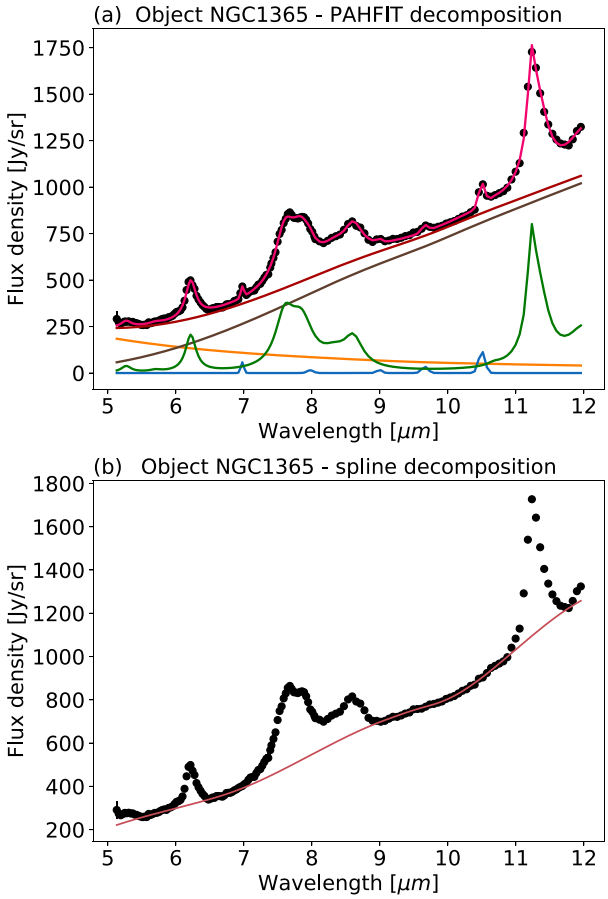

Figure 3. Comparison between the spectral decomposition with PAHFIT and with spline for an object without the PAH plateaus. (a) Result of the PAHFIT decomposition of the 3C31 spectrum. The data points are represented by the dots with the vertical error bars as uncertainties. The pink line corresponds to the best-fitting model, the green line is the dust (AIB, PAH) contribution, and blue one is the ionic and molecular lines contribution. The red line represents the total continuum contribution, and the brown and orange lines correspond to its individual thermal and stellar components, respectively. (b) The red line represents the spline decomposition of the continuum. The data points are represented by the dots with the vertical error bars as uncertainties.

were the values of 6.22 μm for the peak position and 0.187 for the FWHM (Smith et al. 2007). An example of this fit can been seen in Fig. 4 (*top*),

$$I_{\rm gauss} = \frac{A}{\sigma\sqrt{2\pi}} \exp\left(-\frac{(x-\lambda_{\rm c})^2}{2\sigma^2}\right), \quad (1)$$

where A is the amplitude, $\lambda_{\rm c}$ is the central wavelength, and the FWHM is given by FWHM $\sim 2.3548\sigma$,

$$\text{rms(per cent)} = \frac{100}{I_{\rm max}}\sqrt{\frac{1}{N}\sum_{i=1}^{N} x_i^2}, \quad (2)$$

where x_i^2 are the quadratic residues, N the number of data, and $I_{\rm max}$ is the maximum flux intensity in the evaluated range. Rms values lower than 10 per cent indicate an appropriate fit and values lower than 5 per cent indicate a very good fit.

The asymmetry of this specific feature caused the deviation of the fitted peak to redder wavelength and, to handle this, these objects had the data points of the profile's red tail removed from the fit

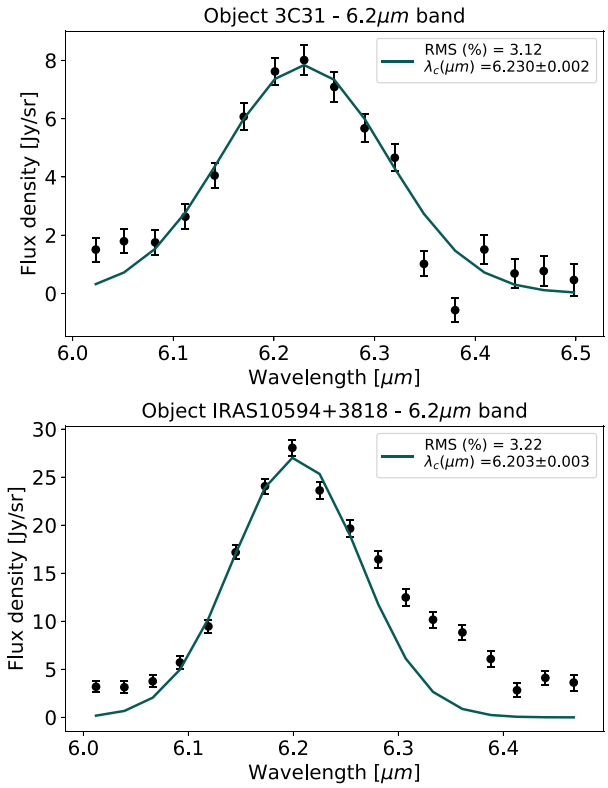

Figure 4. Profile of 6.2 μm band fitted with *curve_fit* for the objects 3C31 (top) and IRAS10594+3818 (bottom). Labels show the values of the peak position and normalized rms. In the case of IRAS10594+3818, the fitting range was reduced to exclude this more evident red tail.

following the same method of Peeters et al. (2017). One possible contributor to this red tail is anharmonic hot-band emission which is a natural consequence of the PAH model, although it is not a major player in determining the profile itself (Hudgins & Allamandola 1999). Some galaxies of our sample required a reduction in the fitting range to better exclude the red tail and they are marked with an asterisk in Table A2. An example of this case is shown in Fig. 4 (bottom).

We also noted the presence of another emission component of the 6.2 μm band near 6.35 μm in some sources and performed the fitting adding a new subcomponent to the 6.22 μm band (Fig. 5, top) in order to compare the two procedures. The inclusion of the second feature seems to encompass the fit for highly asymmetric profiles by reproducing their red tail, previously underestimated in some galaxies, as for the object IRAS10594+3818 (Fig. 5, bottom). Even so, in these situations, there is no real indication of the presence of the second feature and the asymmetry could be just a characteristic of the anharmonic profile (Tielens 2008). In this work, we used only the fitting with just one Gaussian to standardize the analysis.

With peak positions obtained, we were able to group the galaxies into the three Peeters' classes (Table 1). Fig. 6 shows the class distribution.

4 RESULTS AND DISCUSSION

The second feature near 6.35 μm has been attributed in some cases to the inherent asymmetry of the band profile. Nevertheless, its peak position varied from 6.246 to 6.471 μm and there are a few possibilities that could give insight into its nature. According to

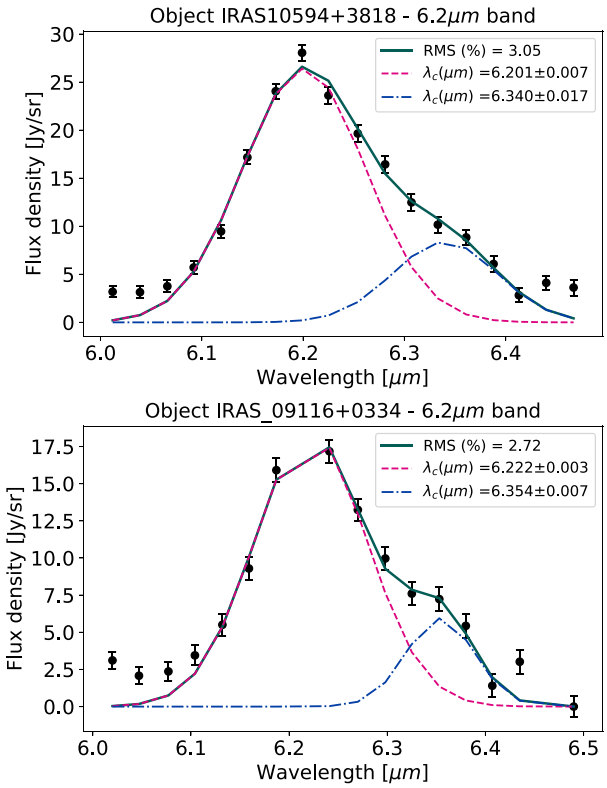

Figure 5. Profile of 6.2 μm band fitted with *curve_fit* for the objects IRAS10594+3818 (top) and IRAS_09116+0334 (bottom) using two different Gaussian profiles. Labels show the values of the peak positions and normalized rms.

Table 1. Intervals for each Peeters' classes (Peeters et al. 2002).

Class	Interval (μm)
A	<6.23
B	$6.23 < \lambda < 6.29$
C	>6.29

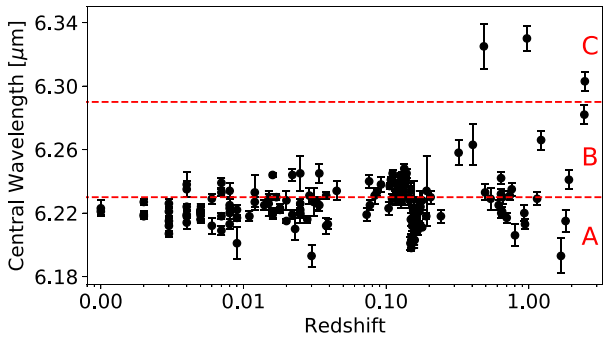

Figure 6. Distribution of the central wavelengths of the 6.2 μm band for the redshift of the sources. The *x*-axis is in logarithmic scale. The dashed lines are the limits among the Peeters' classes, represented also by the letters A, B, and C.

Table 2. Number of galaxies that fall into each Peeters' class.

Galaxies	Class A	Class B	Class C
155	67 per cent	31 per cent	2 per cent

Pino et al. (2008), who performed experiments with PAHs in order to verify the origins of their emissions, bands near 6.3 μm may be related to aliphatic features. On the other hand, the 6.4 μm band observed in the reflection nebula NGC7023 was attributed to the C_{60}^{+} (Berné, Montillaud & Joblin 2015). PAH cations, without any carbon substituted, could also be the responsible for this emission (Hudgins et al. 2005). Finally, peaks at ≈6.41 μm could be due to perylene-like structures (Candian, Sarre & Tielens 2014).

Table 2 summarizes the separation of the 155 objects into Peeters' classes derived from the *curve_fit* fits. Details are given in Table A2. An overview of the results is shown in Fig. 6, which displays the distribution of the central wavelengths taking account of redshifts of the galaxies. There is a small predominance of class A objects over class B objects (more evident for redshifts lower than 0.05). Only three galaxies were classified as C.

Pino et al. (2008) have already noticed that class A objects are the most common in the Universe and embrace several astrophysical sources, while class C objects are in the minority. Our results point to the same conclusions, especially for starburst-dominated sources whose class A members are up to 67 per cent in our study. This evidence is more pronounced at lower redshifts, as can be seen in Fig. 6. In addition, if we consider class B as a mixture between PANH and PAH emissions, as pointed out by Peeters et al. (2002), we can verify that PANHs dominate this subclass of galaxies based on analysis of the 6.2 μm PAH.

Regarding class C, just three objects do not allow us to distinguish any pattern. Apparently, they may be expected in higher redshifts, which might also imply an evolutionary time-scale of PAH molecules. Chemically young astrophysical sources might have reduced PAH abundances and PAH molecules are not as efficiently produced in low-metallicity environments because fewer carbon atoms are available in the ISM (Shivaei et al. 2017). In this case, class C could be represented by very small grains (VSGs). It was already noticed that VSGs may be responsible for the extended red wing and redshift of the peak position of the 11.2 μm PAH band (Rosenberg et al. 2011). Besides, they may also be the carrier of the 7.8 μm subcomponent of the 7.7 μm PAH band and the 8.25 μm component of the 8.6 μm PAH band (Peeters et al. 2017), which are expected to be stronger for class C objects (Section 1). Nevertheless, as the higher redshift objects were extrapolated by the PAH bands themselves and were not corroborated with other spectroscopic or photometric data, any additional analysis may be misguided because the redshift errors can be as large as 0.1–0.2 depending on how many features were used in the calculation (Yan et al. 2007).

According to Ota (2016), the substitution of three or more nitrogen atoms into PAHs does not provide molecules that describe the observed features. This could indicate that compounds of astrobiological interest such as purine and adenine may not be synthesized in the ISM. On the other hand, considering just one or two nitrogen atoms, some species were capable of reproducing the observations ($C_7H_5N_2$-ab^{3+}, for example). However, only small PANHs were considered in their study and they are easily destroyed in the ISM than larger molecules. We can expect that larger PANHs are correlated to the 6.2 μm band emission since PAHs with >20–30 carbon atoms are thought to dominate the emitting interstellar PAHs.

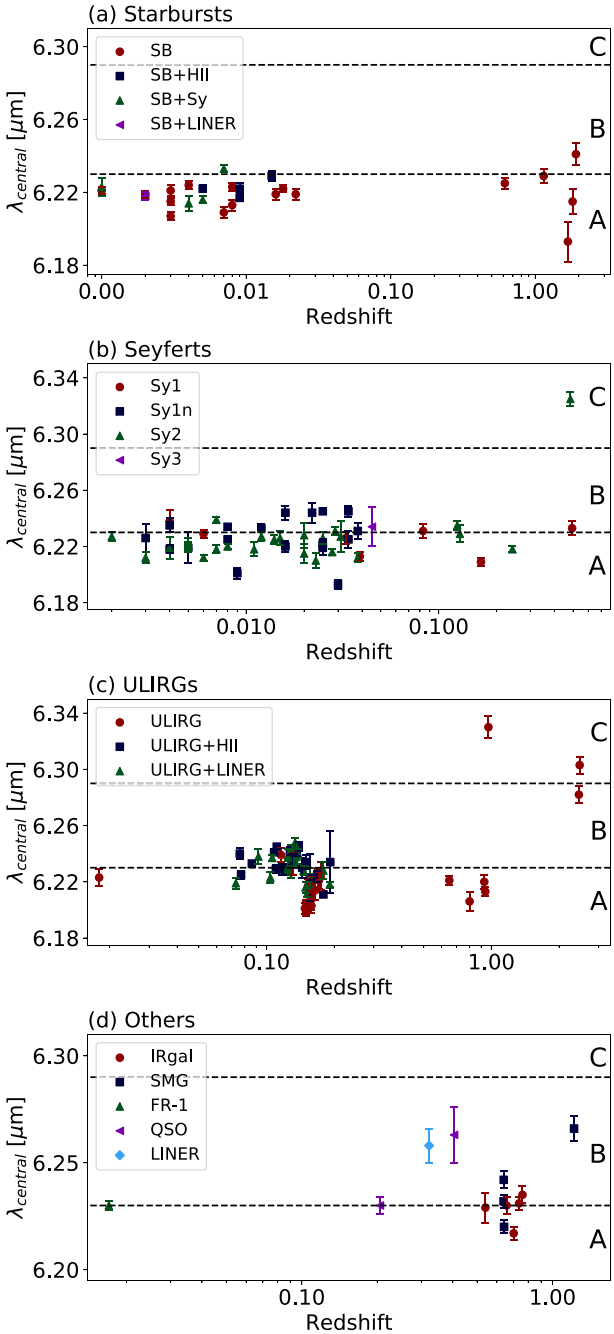

Figure 7. Distribution of the central wavelengths of the 6.2 μm band according to the galaxy type – (a) Starbursts; (b) Seyferts; (c) ULIRGs; and (d) Others. The dashed lines are the limits among the Peeters' classes, indicated also by A, B, or C letter. Acronyms: AGN – active galactic nucleus, FR – Fanaroff–Riley galaxy, H II–H II region, IRgal – Infrared galaxy, LINER – low-ionization nuclear emission-line region, QSO – quasi-stellar object, SB – Starburst galaxy, SMG – submillimetre Galaxy, Sy – Seyfert galaxy, and ULIRG – ultraluminous infrared galaxy.

Fig. 7 illustrates the class distribution in different galaxy types for both methods applied (see Table A1). Table 3 presents the percentages of each class for the three most abundant objects of the galaxies – starbursts (17 per cent), Seyferts (34 per cent), and ULIRGs (41 per cent). The other types comprehend 8 per cent.

Table 3. Peeters' class distribution for starbursts, Seyferts, and ULIRG galaxies.

Object	A (per cent)	B (per cent)	C (per cent)	Total of the sample (per cent)
SB SB + H II SB + Sy	92	8	0	17
Sy1 Sy1n Sy2 Sy3	70	28	2	34
ULIRG ULIRG + H II ULIRG + LINER	59	38	3	41
Others	46	54	0	8

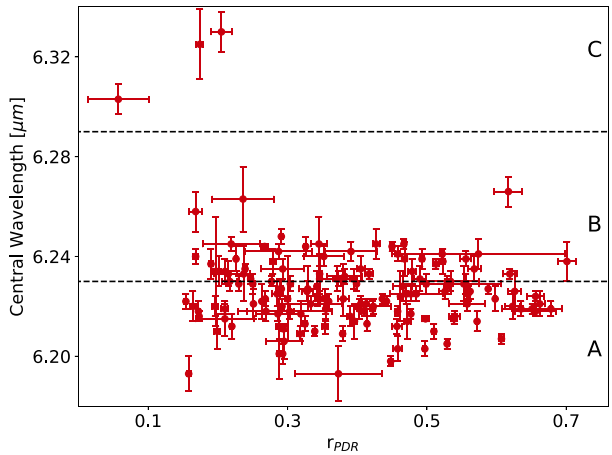

Figure 8. Distribution of the central wavelengths of the 6.2 μm band for the spectral contribution of PDR component r_{PDR} of 152 sources whose values were available in the ATLAS project. The uncertainties are displayed as error bars when available. The dashed lines are the limits among the Peeters' classes, represented also by letters A, B, and C.

In the scenario in which class A 6.2 μm band position arises from PANHs, the importance of these species is greater in starbursts. However, the fact that most of the ULIRGs and Seyferts are class A objects indicates a significant presence of PANHs also in these environments. The prevalence of class A objects in our study could be explained by the dominance of star formation contribution in all sources of our sample, or by the ubiquity of PANHs in galaxies. Studies of samples with a larger number of AGN-dominated sources could help to clarify this issue. Only in SMGs, class B dominates: three in four galaxies are classified as B. Again, more data is needed for further analysis.

Fig. 8 shows the distribution of the central wavelengths of the 6.2 μm band for the spectral contribution of the PDR component (r_{PDR}) of the sources, as calculated by Hernán-Caballero & Hatziminaoglou (2011). The r_{PDR} value is the ratio of the total integrated luminosity to the total luminosity of the PDR component in the 5–15 μm rest-frame range. In this sense, the class C sources present low contribution of star formation and greater contribution of the ANG or H II region components, also calculated by Hernán-Caballero & Hatziminaoglou (2011). Table 4 shows these respective values for the three class C sources.

Table 4. Spectral contribution of the AGN, H II, and PDR components for the class C objects (Hernán-Caballero & Hatziminaoglou 2011).

Object	r_{AGN}	$r_{H\,II}$	r_{PDR}
MIPS 180	0.439 ± 0.075	0.504 ± 0.112	0.057 ± 0.044
SDSS_J00562 1.72+003 235.8	0.571 ± 0.008	0.256 ± 0.006	0.174 ± 0.005
SWIRE4_J1036 37.18+584 217.0	0.458 ± 0.022	0.337 ± 0.014	0.205 ± 0.015

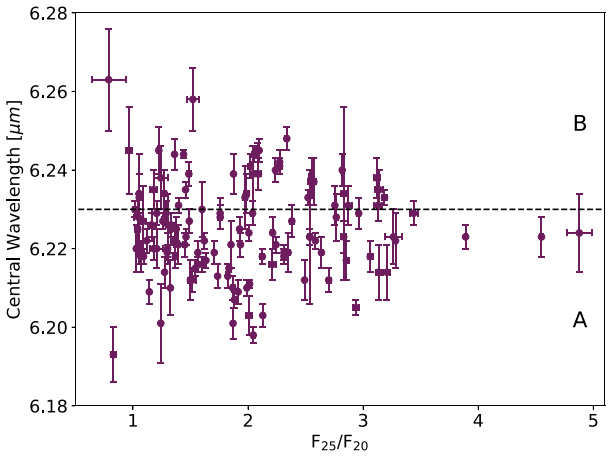

Figure 9. Distribution of the central wavelengths of the 6.2 μm band for the F_{25}/F_{20} ratio of 129 sources whose values were available in the ATLAS project. The uncertainties are displayed as error bars when available. The dashed lines are the limits among the Peeters' classes, represented also by letters A, B, and C.

On the other hand, if we consider the F_{25}/F_{20} ratio (Fig. 9), we can see that class A objects are the coldest. The values of r_{PDR}, F_{25}, and F_{20} together with their respective uncertainties were extracted directly from the ATLAS project when they were available. The uncertainty of the F_{25}/F_{20} ratio was propagated from the F_{25} and F_{20} errors. The values of r_{PDR} and F_{25}/F_{20} ratio can be seen in Table A3.

5 CONCLUSIONS

We have analysed the MIR spectra of 155 starburst-dominated galaxies, searching for the contribution of the Peeters' class A 6.2 μm band to the total sample. To date, the class A position of this band can only be attributed to PANHs, PAHs containing *N* atoms. Thus, the PAH feature profiles, especially the 6.2 μm band, could indicate the presence of nitrogen incorporated to the rings.

The fitted 6.2 μm profiles were classified in classes A, B, and C following Peeters et al. (2002). At 67 per cent of the sample, class A profiles clearly dominate, suggesting a significant presence of PANHs in the ISM of these galaxies. Class B corresponded to a percentage of 31 per cent, indicating a significantly smaller contribution of PANHs in these sources. Only class C, with a small percentage of 2 per cent, seems not to be influenced by these molecules. These trends give support to the suggestion that class A/B 6.2 μm band variations track changes in PANH ionization state or molecular structure (Bauschlicher, Peeters & Allamandola 2009). In addition, we can see that class A objects are colder compared to class B objects.

Within the PANH scenario, the ubiquity of PANHs could indicate another reservoir of nitrogen in the Universe, with density and temperature conditions that differ from those of gas and ices phases. As shown in Fig. 7, they can be present in the ISM of starburst galaxies, ULIRGs, Seyferts, infrared, and submillimetre galaxies. Furthermore, they are responsible for an important fraction of the MIR emission, especially for the 6.2 μm band. These findings also give support to the idea of their contribution to the origins of life on Earth and elsewhere, since they could form nucleobase-type structures in the ISM (Elsila et al. 2006; Parker et al. 2015).

Extension of this analysis to other types of objects also available in the ATLAS project, such as AGNs, could shed light on how the starburst-dominated emission of the sources is responsible for the majority of class A objects and could provide a broader overview of the 6.2 μm band behaviour in astrophysical environments.

Moreover, it will also be possible to explore the other PAH bands in more detail, which could be of great interest to this study. Since 6.2 and 7.7 μm bands are both caused by the CC stretching vibrational mode, they are connected to each other in some cases, mainly for class A (van Diedenhoven et al. 2004). This association could furnish another strategy for deriving the variations of the 6.2 μm band in an indirect way.

The question why the presence of PANHs is more apparent in some galaxies but not in others could be addressed with chemical evolution models taking into account differences in metallicity, star formation history, and the nature of molecular clouds in the harbouring galaxy, e.g. the chemodynamical model in Friaça & Barbuy (2017). In addition, further computational calculations together with laboratory measurements are needed to make more robust predictions of the role of PANHs in the profile of the PAH emission bands, mainly in the conditions prevailing in galaxies with star formation.

ACKNOWLEDGEMENTS

Special acknowledgements to CAPES (Comissão de Aperfeiçoamento de Pessoal do Nível Superior) and CNPq (Conselho Nacional de Desenvolvimento Científico e Tecnológico) for the financial support.

REFERENCES

Allamandola L. J., Hudgins D. M., Sandford S. A., 1999, ApJ, 511, L115
Bauschlicher C. W., Jr, Peeters E., Allamandola L. J., 2009, ApJ, 697, 311
Berné O., Montillaud J., Joblin C., 2015, A&A, 577, A133
Boersma C., Bregman J. D., Allamandola L. J., 2013, ApJ, 769, 117
Boersma C. et al., 2014, ApJS, 211, 8
Brandl B. R. et al., 2006, ApJ, 653, 1129
Buchanan C. L., Gallimore J. F., O'Dea C. P., Baum S. A., Axon D. J., Robinson A., Elitzur M., Elvis M., 2006, AJ, 132, 401
Candian A., Sarre P. J., 2015, MNRAS, 448, 2960
Candian A., Sarre P. J., Tielens A. G. G. M., 2014, ApJ, 791, L10
Dasyra K. M. et al., 2009, ApJ, 701, 1123
Deo R. P., Crenshaw D. M., Kraemer S. B., Dietrich M., Elitzur M., Teplitz H., Turner T. J., 2007, ApJ, 671, 124
Draine B. T., Li A., 2001, in American Astronomical Society Meeting Abstracts. p. 1451
Draine B. T., Li A., 2007, ApJ, 657, 810
Ehrenfreund P. et al., 2002, Rep. Prog. Phys., 65, 1427
Ehrenfreund P., Rasmussen S., Cleaves J., Chen L., 2006, Astrobiology, 6, 490
Elsila J. E., Hammond M. R., Bernstein M. P., Sandford S. A., Zare R. N., 2006, Meteorit. Planet. Sci., 41, 785
Farrah D., Weedman D., Lonsdale C. J., Polletta M., Rowan-Robinson M., Houck J., Smith H. E., 2009, ApJ, 696, 2044
Friaça A. C. S., Barbuy B., 2017, A&A, 598, A121

Galliano F., Madden S. C., Tielens A. G. G. M., Peeters E., Jones A. P., 2008, ApJ, 679, 310
Genzel R., Cesarsky C. J., 2000, ARA&A, 38, 761
Hernán-Caballero A., Hatziminaoglou E., 2011, MNRAS, 414, 500
Hernán-Caballero A. et al., 2009, MNRAS, 395, 1695
Hiner K. D., Canalizo G., Lacy M., Sajina A., Armus L., Ridgway S., Storrie-Lombardi L., 2009, ApJ, 706, 508
Houck J. R. et al., 2004, ApJS, 154, 18
Hudgins D. M., Allamandola L. J., 1999, ApJ, 513, L69
Hudgins D. M., Bauschlicher C. W., Jr, Allamandola L. J., 2005, ApJ, 632, 316
Imanishi M., 2009, ApJ, 694, 751
Imanishi M., Dudley C. C., Maiolino R., Maloney P. R., Nakagawa T., Risaliti G., 2007, ApJS, 171, 72
Imanishi M., Maiolino R., Nakagawa T., 2010, ApJ, 709, 801
Joblin C., Leger A., Martin P., 1992, ApJ, 393, L79
Leipski C., Antonucci R., Ogle P., Whysong D., 2009, ApJ, 701, 891
Li A., 2004, in Witt A. N., Clayton G. C., Draine B. T., eds, ASP Conf. Ser. Vol. 309, Astrophysics of Dust. Astron. Soc. Pac., San Francisco, p. 417
Murphy E. J., Chary R.-R., Alexander D. M., Dickinson M., Magnelli B., Morrison G., Pope A., Teplitz H. I., 2009, ApJ, 698, 1380
Ota N., 2016, preprint (arXiv:1603.03399)
Papovich C. et al., 2006, ApJ, 640, 92
Parker D. S. N., Kaiser R. I., Kostko O., Troy T. P., Ahmed M., Mebel A. M., Tielens A. G. G. M., 2015, ApJ, 803, 53
Peeters E., Hony S., Van Kerckhoven C., Tielens A. G. G. M., Allamandola L. J., Hudgins D. M., Bauschlicher C. W., 2002, A&A, 390, 1089
Peeters E., Bauschlicher C. W., Jr, Allamandola L. J., Tielens A. G. G. M., Ricca A., Wolfire M. G., 2017, ApJ, 836, 198
Pino T. et al., 2008, A&A, 490, 665
Pope A. et al., 2008, ApJ, 675, 1171
Riechers D. A. et al., 2014, ApJ, 786, 31
Rosenberg M. J. F., Berné O., Boersma C., Allamandola L. J., Tielens A. G. G. M., 2011, A&A, 532, A128
Sales D. A., Pastoriza M. G., Riffel R., Winge C., 2012, MNRAS, 429, 2634
Shi Y. et al., 2006, ApJ, 653, 127
Shivaei I. et al., 2017, ApJ, 837, 157
Siana B. et al., 2009, ApJ, 698, 1273
Smith J. D. T. et al., 2007, ApJ, 656, 770
Sturm E., Hasinger G., Lehmann I., Mainieri V., Genzel R., Lehnert M. D., Lutz D., Tacconi L. J., 2006, ApJ, 642, 81
Teplitz H. I. et al., 2007, ApJ, 659, 941
Tielens A. G. G. M., 2008, ARA&A, 46, 289
van Diedenhoven B., Peeters E., Van Kerckhoven C., Hony S., Hudgins D. M., Allamandola L. J., Tielens A. G. G. M., 2004, ApJ, 611, 928
Weedman D. W., Houck J. R., 2009, ApJ, 693, 370
Weedman D. W. et al., 2005, ApJ, 633, 706
Weedman D. et al., 2006, ApJ, 653, 101
Werner M. W. et al., 2004, ApJS, 154, 1
Wu Y., Charmandaris V., Huang J., Spinoglio L., Tommasin S., 2009, ApJ, 701, 658
Yan L. et al., 2005, ApJ, 628, 604
Yan L. et al., 2007, ApJ, 658, 778
Zakamska N. L., Gómez L., Strauss M. A., Krolik J. H., 2008, AJ, 136, 1607

APPENDIX A: SOURCES – IDENTIFICATION AND DERIVED PROPERTIES

Table A1. Sources and their respective information extracted from the MIR_SB sample (*Spitzer*/IRS ATLAS, version 1.0) and Yan et al. (2007), including their ID, type, source reference, right ascension, declination, and redshift. Acronyms: AGN – active galactic nucleus, FR – Fanaroff-Riley galaxy, H II–H II region, IRgal – Infrared galaxy, LINER – low-ionization nuclear emission-line region, QSO – quasi-stellar object, SB – Starburst galaxy, SMG – submillimetre Galaxy, Sy – Seyfert galaxy, and ULIRG – ultraluminous infrared galaxy.

ID	Type	Reference	RA (hms)	Dec. (dms)	z
3C293	Sy3	Leipski et al. (2009)	13:52:17.80	31:26:46.50	0.045
3C31	FR-1	Leipski et al. (2009)	01:07:24.90	32:24:45.20	0.017
AGN15[a]	LINER	Weedman & Houck (2009)	17:18:52.71	59:14:32.00	0.322
Arp220	ULIRG	Imanishi et al. (2007)	15:34:57.10	23:30:11.00	0.018
CGCG381-051	Sy2	Wu et al. (2009)	23:48:41.70	02:14:23.00	0.031
E12-G21	Sy1	Wu et al. (2009)	00:40:47.80	−79:14:27.00	0.033
EIRS-2[a]	SB	Hernán-Caballero et al. (2009)	16:13:49.94	54:26:28.40	1.143
EIRS-14[a]	SB	Hernán-Caballero et al. (2009)	16:35:36.64	40:47:53.80	0.615
EIRS-41	QSO	Hernán-Caballero et al. (2009)	16:34:28.15	41:27:42.60	0.405
GN26	SMG	Pope et al. (2008)	12:36:34.51	62:12:40.90	1.219
IC342	SB	Brandl et al. (2006)	03:46:48.51	68:05:46.00	0.001
IRAS02021−2103	ULIRG	Imanishi, Maiolino & Nakagawa (2010)	02:04:27.30	−20:49:41	0.116
IRAS02480−3745	ULIRG	Imanishi et al. (2010)	02:50:01.70	−37:32:45	0.165
IRAS03209−0806	Sy1	Imanishi et al. (2010)	03:23:22.90	−07:56:15	0.166
IRAS04074−2801	ULIRG	Imanishi et al. (2010)	04:09:30.40	−27:53:44	0.153
IRAS05020−2941	ULIRG	Imanishi et al. (2010)	05:04:00.70	−29:36:55	0.154
IRAS08591+5248	ULIRG	Imanishi et al. (2010)	09:02:47.50	52:36:30	0.158
IRAS10594+3818	ULIRG	Imanishi et al. (2010)	11:02:14.00	38:02:35	0.158
IRAS12447+3721	ULIRG	Imanishi et al. (2010)	12:47:07.70	37:05:37	0.158
IRAS13106−0922	ULIRG	Imanishi et al. (2010)	13:13:14.80	−09:38:00	0.174
IRAS14121−0126	ULIRG	Imanishi et al. (2010)	14:14:45.50	−01:40:55	0.150
IRAS14197+0813	ULIRG	Imanishi et al. (2010)	14:22:11.60	07:59:28AM	0.131
IRAS14202+2615	ULIRG	Imanishi et al. (2010)	14:22:31.40	26:02:05	0.159
IRAS14485−2434	ULIRG	Imanishi et al. (2010)	14:51:23.80	−24:46:30	0.148
IRAS15043+5754	ULIRG	Imanishi et al. (2010)	15:05:39.50	57:43:07	0.150
IRAS21477+0502	ULIRG	Imanishi et al. (2010)	21:50:16.30	05:16:03AM	0.171
IRAS22088−1831	ULIRG	Imanishi et al. (2010)	22:11:33.80	−18:17:06	0.170

Table A1 – *continued*

ID	Type	Reference	RA (hms)	Dec. (dms)	z
IRAS_00091−0738	ULIRG + H II	Imanishi et al. (2007)	00:11:43.30	−07:22:07.00	0.118
IRAS_00456−2904	ULIRG + H II	Imanishi et al. (2007)	00:48:06.80	−28:48:19.00	0.110
IRAS_01199−2307	ULIRG + H II	Imanishi (2009)	01:22:20.90	−22:52:07.00	0.156
IRAS_01355−1814	ULIRG + H II	Imanishi (2009)	01:37:57.40	−17:59:21.00	0.192
IRAS_01494−1845	ULIRG	Imanishi (2009)	01:51:51.40	−18:30:46.00	0.158
IRAS_02411+0353	ULIRG + H II	Imanishi et al. (2007)	02:43:46.10	04:06:37.00	0.144
IRAS_03250+1606	ULIRG + LINER	Imanishi et al. (2007)	03:27:49.80	16:17:00.00	0.129
IRAS_03521+0028	ULIRG + LINER	Imanishi (2009)	03:54:42.20	00:37:03.00	0.152
IRAS_08201+2801	ULIRG + H II	Imanishi (2009)	08:23:12.60	27:51:40.00	0.168
IRAS_09039+0503	ULIRG + LINER	Imanishi et al. (2007)	09:06:34.20	04:51:25.00	0.125
IRAS_09116+0334	ULIRG + LINER	Imanishi et al. (2007)	09:14:13.80	03:22:01.00	0.146
IRAS_09463+8141	ULIRG + LINER	Imanishi (2009)	09:53:00.50	81:27:28.00	0.156
IRAS_09539+0857	Sy2	Imanishi et al. (2007)	09:56:34.30	08:43:06.00	0.129
IRAS_10190+1322	ULIRG + H II	Imanishi et al. (2007)	10:21:42.50	13:06:54.00	0.077
IRAS_10485−1447	ULIRG + LINER	Imanishi et al. (2007)	10:51:03.10	−15:03:22.00	0.133
IRAS_10494+4424	ULIRG + LINER	Imanishi et al. (2007)	10:52:23.50	44:08:48.00	0.092
IRAS_11130−2659	ULIRG + LINER	Imanishi et al. (2007)	11:15:31.60	−27:16:23.00	0.136
IRAS_11387+4116	ULIRG + H II	Imanishi et al. (2007)	11:41:22.00	40:59:51.00	0.149
IRAS_11506+1331	ULIRG + H II	Imanishi et al. (2007)	11:53:14.20	13:14:28.00	0.127
IRAS_12112+0305	ULIRG + LINER	Imanishi et al. (2007)	12:13:46.00	02:48:38.00	0.073
IRAS_12359−0725	ULIRG + LINER	Imanishi et al. (2007)	12:38:31.60	−07:42:25.00	0.138
IRAS_13335−2612	ULIRG + LINER	Imanishi et al. (2007)	13:36:22.30	−26:27:34.00	0.125
IRAS_13469+5833	ULIRG + H II	Imanishi (2009)	13:48:40.20	58:18:52.00	0.158
IRAS_13509+0442	ULIRG + H II	Imanishi et al. (2007)	13:53:31.60	04:28:05.00	0.136
IRAS_13539+2920	ULIRG + H II	Imanishi et al. (2007)	13:56:10.00	29:05:35.00	0.108
IRAS_14060+2919	ULIRG + H II	Imanishi et al. (2007)	14:08:19.00	29:04:47.00	0.117
IRAS_14252−1550	ULIRG + LINER	Imanishi et al. (2007)	14:28:01.10	−16:03:39.00	0.149
IRAS_14348−1447	Sy1	Imanishi et al. (2007)	14:37:38.30	−15:00:23.00	0.083
IRAS_15206+3342	Sy2	Imanishi et al. (2007)	15:22:38.00	33:31:36.00	0.125
IRAS_15225+2350	ULIRG + H II	Imanishi et al. (2007)	15:24:43.90	23:40:10.00	0.139
IRAS_16090−0139	ULIRG + LINER	Imanishi et al. (2007)	16:11:40.50	−01:47:06.00	0.134
IRAS_16300+1558	Sy2	Imanishi (2009)	16:32:21.40	15:51:46.00	0.242
IRAS_16333+4630	ULIRG + LINER	Imanishi (2009)	16:34:52.60	46:24:53.00	0.191
IRAS_16474+3430	ULIRG + H II	Imanishi et al. (2007)	16:49:14.20	34:25:10.00	0.111
IRAS_16487+5447	ULIRG + LINER	Imanishi et al. (2007)	16:49:47.00	54:42:35.00	0.104
IRAS_17028+5817	ULIRG + LINER	Imanishi et al. (2007)	17:03:41.90	58:13:45.00	0.106
IRAS_17068+4027	ULIRG + H II	Imanishi (2009)	17:08:31.90	40:23:28.00	0.179
IRAS_20414−1651	ULIRG + H II	Imanishi et al. (2007)	20:44:18.20	−16:40:16.00	0.086
IRAS_21208−0519	ULIRG + H II	Imanishi et al. (2007)	21:23:29.10	−05:06:56.00	0.130
IRAS_21329−2346	ULIRG + LINER	Imanishi et al. (2007)	21:35:45.80	−23:32:35.00	0.125
IRAS_22206−2715	ULIRG + H II	Imanishi et al. (2007)	22:23:28.90	−27:00:04.00	0.132
IRAS_22491−1808	ULIRG + H II	Imanishi et al. (2007)	22:51:49.20	−17:52:23.00	0.076
IRAS_23129+2548	ULIRG + LINER	Imanishi (2009)	23:15:21.40	26:04:32.00	0.179
IRAS_23234+0946	ULIRG + LINER	Imanishi et al. (2007)	23:25:56.20	10:02:49.00	0.128
LH_H901A	QSO2	Sturm et al. (2006)	10:52:52.80	57:29:00.00	0.205
M-2-40-4	Sy1.9	Wu et al. (2009)	15:48:24.90	−13:45:28.00	0.025
M-5-13-17	Sy1.5	Wu et al. (2009)	05:19:35.80	−32:39:28.00	0.012
M+0-29-23	Sy2	Wu et al. (2009)	11:21:12.20	−02:59:03.00	0.025
MIPS180[a]	ULIRG	Yan et al. (2007)	17:15:43.54	58:35:31.20	2.470
MIPS562	IRgal	Dasyra et al. (2009)	17:12:39.60	58:59:55.10	0.540
MIPS8040	IRgal	Dasyra et al. (2009)	17:13:12.00	60:08:40.20	0.759
MIPS8242[a]	ULIRG	Yan et al. (2007)	17:14:33.17	59:39:11.20	2.450
MIPS15755	IRgal	Dasyra et al. (2009)	17:18:34.90	59:45:34.10	0.736
MIPS22307	IRgal	Dasyra et al. (2009)	17:19:51.40	58:42:22.80	0.700
MIPS22352	IRgal	Dasyra et al. (2009)	17:21:47.70	58:53:55.90	0.656
Mrk52	SB	Brandl et al. (2006)	12:25:42.67	00:34:20.40	0.007
Mrk273	Sy2	Wu et al. (2009)	13:44:42.10	55:53:13.00	0.038
Mrk334	Sy1.8	Deo et al. (2007)	00:03:09.60	21:57:37.00	0.022
Mrk471	Sy1.8	Deo et al. (2007)	14:22:55.40	32:51:03.00	0.034
Mrk609	Sy1.8	Deo et al. (2007)	03:25:25.30	−06:08:38.00	0.034
Mrk622	Sy2	Deo et al. (2007)	08:07:41.00	39:00:15.00	0.023
Mrk883	Sy1.9	Deo et al. (2007)	16:29:52.90	24:26:38.00	0.038
Mrk938	Sy2	Wu et al. (2009)	00:11:06.50	−12:06:26.00	0.020
Mrk1066	Sy2	Shi et al. (2006)	02:59:58.60	36:49:14.00	0.012

Table A1 – *continued*

ID	Type	Reference	RA (hms)	Dec. (dms)	z
Murphy3	SMG	Murphy et al. (2009)	12:36:03.25	62:11:10.80	0.638
Murphy8	SMG	Murphy et al. (2009)	12:36:22.48	62:15:44.30	0.639
Murphy22	SMG	Murphy et al. (2009)	12:37:34.52	62:17:23.20	0.641
NGC513	Sy2	Wu et al. (2009)	01:24:26.80	33:47:58.0	0.02
NGC520	SB + Sy1.8	Brandl et al. (2006)	01:24:35.07	03:47:32.7	0.0071
NGC660	SB	Brandl et al. (2006)	01:43:02.45	13:38:44.4	0.0029
NGC1056	Sy2	Wu et al. (2009)	02:42:48.30	28:34:27.00	0.005
NGC1097	SB + Sy1	Wu et al. (2009)	02:46:19.08	−30:16:28.00	0.004
NGC1125	Sy2	Wu et al. (2009)	02:51:40.30	−16:39:04.00	0.011
NGC1143	Sy2	Wu et al. (2009)	02:55:12.20	−00:11:01.00	0.029
NGC1222	SB	Brandl et al. (2006)	03:08:56.74	−02:57:18.50	0.008
NGC1365	SB + Sy1.8	Brandl et al. (2006)	03:33:36.37	−36:08:25.50	0.005
NGC1566	Sy1.5	Wu et al. (2009)	04:20:00.40	−54:56:16.00	0.005
NGC1614	SB + H II	Brandl et al. (2006)	04:33:59.85	−08:34:44.00	0.015
NGC1667	Sy2	Wu et al. (2009)	04:48:37.10	−06:19:12.00	0.015
NGC2146	SB	Brandl et al. (2006)	06:18:37.71	78:21:25.30	0.004
NGC2273	Sy1	Shi et al. (2006)	06:50:08.60	60:50:45.00	0.006
NGC2623	SB	Brandl et al. (2006)	08:38:24.08	25:45:16.90	0.018
NGC2992	Sy1.9	Wu et al. (2009)	09:45:42.00	−14:19:35.00	0.008
NGC3079	Sy2	Weedman et al. (2005)	10:01:57.80	55:40:47.00	0.004
NGC3227	Sy1.5	Wu et al. (2009)	10:23:30.60	19:51:54.00	0.004
NGC3256	SB	Brandl et al. (2006)	10:27:51.27	−43:54:13.80	0.008
NGC3310	SB + H II	Brandl et al. (2006)	10:38:45.96	53:30:12.00	0.005
NGC3511	Sy1	Wu et al. (2009)	11:03:23.80	−23:05:12.00	0.004
NGC3556	SB	Brandl et al. (2006)	11:11:30.97	55:40:26.80	0.003
NGC3628	SB + LINER	Brandl et al. (2006)	11:20:17.02	13:35:22.20	0.002
NGC3786	Sy1.8	Deo et al. (2007)	11:39:42.50	31:54:33.00	0.009
NGC3982	Sy1.9	Wu et al. (2009)	11:56:28.10	55:07:31.00	0.004
NGC4088	SB	Brandl et al. (2006)	12:05:34.19	50:32:20.50	0.003
NGC4194	SB + H II	Brandl et al. (2006)	12:14:09.64	54:31:34.60	0.009
NGC4388	Sy2	Wu et al. (2009)	12:25:46.70	12:39:44.00	0.008
NGC4676	SB	Brandl et al. (2006)	12:46:10.10	30:43:55.00	0.022
NGC4818	SB	Brandl et al. (2006)	12:56:48.90	−08:31:31.10	0.002
NGC4945	SB + Sy2	Brandl et al. (2006)	13:05:27.48	−49:28:05.60	0.001
NGC5005	Sy2	Wu et al. (2009)	13:10:56.20	37:03:33.00	0.003
NGC5033	Sy1.8	Wu et al. (2009)	13:13:27.50	36:35:38.00	0.003
NGC5135	Sy2	Wu et al. (2009)	13:25:44.00	-29:50:01.00	0.014
NGC5194	Sy2	Wu et al. (2009)	13:29:52.70	47:11:43.00	0.002
NGC5256	Sy2	Wu et al. (2009)	13:38:17.50	48:16:37.00	0.028
NGC5674	Sy1.9	Shi et al. (2006)	14:33:52.20	05:27:30.00	0.025
NGC5953	Sy2	Buchanan et al. (2006)	15:34:32.40	15:11:38.00	0.007
NGC6810	Sy2	Wu et al. (2009)	19:43:34.40	−58:39:21.00	0.007
NGC6890	Sy1.9	Wu et al. (2009)	20:18:18.10	−44:48:25.00	0.008
NGC7130	Sy1.9	Buchanan et al. (2006)	21:48:19.50	−34:57:05.00	0.016
NGC7252	SB	Brandl et al. (2006)	22:20:44.77	−24:40:41.80	0.016
NGC7469	Sy1.5	Wu et al. (2009)	23:03:15.60	08:52:26.00	0.016
NGC7496	Sy2	Buchanan et al. (2006)	23:09:47.30	−43:25:41.00	0.006
NGC7582	Sy2	Wu et al. (2009)	23:18:23.50	−42:22:14.00	0.005
NGC7590	Sy2	Wu et al. (2009)	23:18:55.00	−42:14:17.00	0.005
NGC7603	Sy1.5	Wu et al. (2009)	23:18:56.60	00:14:38.00	0.030
NGC7714	SB + H II	Brandl et al. (2006)	23:36:14.10	02:09:18.60	0.009
SDSS_J005621.72+003235.8	Sy2	Zakamska et al. (2008)	00:56:21.72	00:32:35.80	0.484
SJ103837.03+582214.8[a]	SB	Weedman et al. (2006)	10:38:37.03	58:22:14.80	1.680
SJ104217.17+575459.2[a]	SB	Weedman et al. (2006)	10:42:17.17	57:54:59.20	1.910
SJ104731.08+581016.1[a]	SB	Weedman et al. (2006)	10:47:31.08	58:10:16.10	1.810
SST172458.3+591545	Sy1	Hiner et al. (2009)	17:24:58.30	59:15:45	0.494
SWIRE4_J103637.18+584217.0[a]	ULIRG	Farrah et al. (2009)	10:36:37.18	58:42:17.00	0.970
SWIRE4_J104057.84+565238.9[a]	ULIRG	Farrah et al. (2009)	10:40:57.84	56:52:38.90	0.930
SWIRE4_J104117.93+595822.9[a]	ULIRG	Farrah et al. (2009)	10:41:17.93	59:58:22.90	0.650
SWIRE4_J104830.58+591810.2	ULIRG	Farrah et al. (2009)	10:48:30.58	59:18:10.20	0.940
SWIRE4_J105943.83+572524.9[a]	ULIRG	Farrah et al. (2009)	10:59:43.83	57:25:24.90	0.800
UGC5101	Sy1	Wu et al. (2009)	09:35:51.60	61:21:11.00	0.039
UGC7064	Sy1.9	Wu et al. (2009)	12:04:43.30	31:10:38.00	0.025
UGC12138	Sy1.8	Deo et al. (2007)	22:40:17.00	08:03:14.00	0.025

[a]Objects with redshift obtained through the IRS spectrum.

Table A2. Best-fitting results for the 6.2 μm band utilizing *curve_fit* and equation (1) (Section 3.1). *A* is the amplitude, λ_c is the central wavelength, and FWHM is the full width at half-maximum.

Source	Class	*A* (Jy sr^{-1})	Err *A* (Jy sr^{-1})	λ_c (μm)	Err λ_c (μm)	FWHM	Err FWHM	rms (%)
3C293	B	0.695	0.049	6.234	0.006	0.175	0.015	7.155
3C31	A	1.611	0.043	6.230	0.002	0.193	0.007	3.120
AGN15	B	0.453	0.037	6.258	0.008	0.209	0.021	5.692
Arp220	A	35.186	1.446	6.223	0.003	0.164	0.009	4.986
CGCG381-051	A	7.201	0.839	6.227	0.009	0.149	0.021	12.127
E12-G21	A	14.414	0.794	6.226	0.004	0.162	0.011	6.058
EIRS-14	A	0.208	0.008	6.225	0.003	0.202	0.010	2.937
EIRS-2*	A	0.181	0.011	6.229	0.004	0.135	0.011	6.905
EIRS-41	B	0.118	0.023	6.263	0.013	0.155	0.036	11.921
GN26	B	0.155	0.012	6.266	0.006	0.154	0.014	5.712
IC342*	A	39.660	1.254	6.221	0.002	0.134	0.005	3.527
IRAS02021-2103*	B	3.261	0.165	6.239	0.005	0.189	0.011	4.195
IRAS02480−3745*	A	2.701	0.184	6.214	0.007	0.203	0.017	5.412
IRAS03209−0806*	A	2.506	0.098	6.209	0.003	0.147	0.007	4.738
IRAS04074−2801*	A	1.447	0.113	6.217	0.005	0.144	0.014	7.855
IRAS05020−2941*	A	1.632	0.200	6.214	0.007	0.115	0.017	13.094
IRAS08591+5248*	A	2.224	0.098	6.210	0.003	0.144	0.008	4.428
IRAS10594+3818*	A	4.092	0.161	6.203	0.003	0.142	0.007	3.221
IRAS12447+3721	A	1.968	0.120	6.219	0.005	0.167	0.012	4.497
IRAS13106−0922	A	1.021	0.127	6.224	0.010	0.166	0.025	15.227
IRAS14121−0126*	A	2.751	0.084	6.198	0.002	0.109	0.004	2.837
IRAS14197+0813	B	1.203	0.153	6.233	0.008	0.121	0.016	9.285
IRAS14202+2615	A	5.443	0.188	6.210	0.002	0.151	0.006	4.393
IRAS14485−2434*	A	2.063	0.130	6.201	0.004	0.123	0.010	5.812
IRAS15043+5754*	A	2.390	0.066	6.205	0.002	0.134	0.005	2.762
IRAS21477+0502	A	1.702	0.140	6.221	0.006	0.159	0.015	10.208
IRAS22088−1831	A	1.284	0.102	6.222	0.007	0.171	0.017	10.250
IRAS_00091−0738*	A	0.812	0.073	6.229	0.004	0.083	0.009	6.277
IRAS_00456−2904*	A	5.286	0.224	6.229	0.003	0.132	0.008	2.837
IRAS_01199−2307	A	1.390	0.339	6.223	0.017	0.143	0.042	12.177
IRAS_01355−1814	B	1.005	0.232	6.234	0.022	0.194	0.053	12.971
IRAS_01494−1845*	A	1.656	0.140	6.203	0.005	0.111	0.011	7.864
IRAS_02411+0353*	A	3.782	0.409	6.230	0.007	0.124	0.015	5.021
IRAS_03250+1606	B	2.986	0.095	6.244	0.002	0.146	0.006	2.936
IRAS_03521+0028*	A	1.724	0.086	6.212	0.003	0.152	0.010	4.857
IRAS_08201+2801	A	2.126	0.092	6.224	0.004	0.191	0.011	3.149
IRAS_09039+0503*	B	1.037	0.096	6.231	0.005	0.119	0.014	6.377
IRAS_09116+0334	A	2.959	0.127	6.228	0.003	0.162	0.009	5.452
IRAS_09463+8141	A	0.970	0.092	6.223	0.007	0.147	0.017	4.404
IRAS_09539+0857	A	1.073	0.054	6.229	0.003	0.141	0.009	5.355
IRAS_10190+1322*	A	11.248	0.452	6.225	0.003	0.162	0.008	3.899
IRAS_10485−1447	B	1.554	0.120	6.237	0.006	0.159	0.014	7.475
IRAS_10494+4424	B	5.380	0.333	6.238	0.005	0.153	0.011	5.899
IRAS_11130−2659*	B	0.785	0.079	6.238	0.005	0.107	0.013	8.459
IRAS_11387+4116	B	1.466	0.105	6.234	0.005	0.135	0.012	5.900
IRAS_11506+1331*	B	3.769	0.150	6.242	0.003	0.138	0.007	2.846
IRAS_12112+0305*	A	5.955	0.461	6.219	0.004	0.123	0.012	3.856
IRAS_12359−0725	B	1.091	0.059	6.240	0.003	0.139	0.010	5.229
IRAS_13335−2612*	B	3.467	0.156	6.239	0.004	0.177	0.009	4.648
IRAS_13469+5833	A	1.186	0.036	6.223	0.002	0.150	0.005	2.225
IRAS_13509+0442*	B	2.571	0.118	6.241	0.003	0.130	0.008	4.209
IRAS_13539+2920	B	4.008	0.111	6.241	0.002	0.142	0.005	2.954
IRAS_14060+2919*	A	4.536	0.302	6.229	0.004	0.138	0.012	4.740
IRAS_14252−1550*	A	1.482	0.092	6.216	0.004	0.151	0.012	5.129
IRAS_14348−1447	B	6.712	0.419	6.231	0.005	0.170	0.014	5.871
IRAS_15206+3342*	B	3.895	0.169	6.235	0.002	0.117	0.006	3.030
IRAS_15225+2350*	B	1.409	0.092	6.245	0.003	0.107	0.009	4.177
IRAS_16090−0139	B	3.432	0.139	6.248	0.003	0.153	0.008	3.864
IRAS_16300+1558	A	1.091	0.062	6.218	0.004	0.140	0.010	4.454
IRAS_16333+4630	A	1.812	0.068	6.218	0.002	0.122	0.005	4.118
IRAS_16474+3430*	B	4.680	0.169	6.245	0.002	0.143	0.006	2.260
IRAS_16487+5447*	A	1.361	0.116	6.223	0.004	0.102	0.010	5.914

Table A2 – *continued*

Source	Class	A (Jy sr^{-1})	Err A (Jy sr^{-1})	λ_c (μm)	Err λ_c (μm)	FWHM	Err FWHM	rms (%)
IRAS_17028+5817*	B	2.479	0.074	6.237	0.002	0.138	0.005	2.784
IRAS_17068+4027*	A	2.280	0.045	6.211	0.001	0.153	0.004	2.082
IRAS_20414−1651	B	2.495	0.086	6.233	0.002	0.133	0.006	3.963
IRAS_21208−0519*	B	2.247	0.206	6.239	0.007	0.174	0.021	8.246
IRAS_21329−2346*	B	1.100	0.077	6.231	0.004	0.117	0.010	5.661
IRAS_22206−2715	B	1.472	0.115	6.235	0.005	0.118	0.012	6.316
IRAS_22491−1808	B	4.206	0.271	6.240	0.004	0.127	0.009	4.841
IRAS_23129+2548	A	1.533	0.111	6.228	0.006	0.173	0.016	9.015
IRAS_23234+0946	A	1.550	0.087	6.227	0.004	0.164	0.012	6.789
LH_H901A	A	0.119	0.006	6.230	0.004	0.159	0.010	5.777
M+0-29-23	A	25.504	0.864	6.226	0.003	0.163	0.007	4.229
M-2-40-4	A	11.328	0.820	6.220	0.006	0.173	0.016	8.827
M-5-13-17	B	12.566	1.449	6.233	0.011	0.250	0.036	7.829
MIPS180*	C	0.137	0.006	6.303	0.006	0.320	0.016	10.540
MIPS562	A	0.228	0.019	6.229	0.007	0.185	0.020	6.512
MIPS8040	B	0.174	0.010	6.235	0.004	0.132	0.009	5.225
MIPS8242*	B	0.050	0.004	6.282	0.006	0.146	0.014	9.851
MIPS15755	B	0.223	0.010	6.231	0.003	0.156	0.009	4.730
MIPS22307*	A	0.115	0.007	6.217	0.003	0.090	0.006	4.758
MIPS22352	A	0.324	0.013	6.230	0.004	0.225	0.012	4.023
Mrk52*	A	12.490	0.481	6.209	0.003	0.146	0.007	3.900
Mrk273*	A	11.823	0.976	6.212	0.005	0.130	0.013	7.593
Mrk334	B	16.966	0.760	6.244	0.004	0.156	0.009	3.191
Mrk471	B	3.212	0.231	6.245	0.006	0.181	0.015	3.970
Mrk609	A	10.671	0.479	6.225	0.004	0.164	0.009	4.127
Mrk622	A	2.439	0.234	6.210	0.007	0.141	0.016	6.779
Mrk883	B	2.445	0.061	6.231	0.002	0.174	0.005	2.178
Mrk938*	A	32.861	0.501	6.215	0.001	0.134	0.002	1.422
Mrk1066	A	19.651	0.593	6.227	0.003	0.205	0.008	3.265
Murphy3	B	0.183	0.006	6.232	0.003	0.188	0.008	3.300
Murphy8	B	0.088	0.004	6.242	0.004	0.171	0.009	3.463
Murphy22	A	0.139	0.005	6.220	0.003	0.190	0.009	3.316
NGC513*	A	11.852	1.162	6.228	0.006	0.179	0.024	6.312
NGC520*	B	65.937	1.346	6.233	0.002	0.148	0.004	2.020
NGC660*	A	139.918	4.928	6.221	0.003	0.154	0.007	4.166
NGC1056*	A	33.577	2.062	6.221	0.005	0.155	0.012	5.681
NGC1097*	A	117.594	5.763	6.214	0.004	0.163	0.010	3.869
NGC1125	A	7.325	0.305	6.218	0.003	0.139	0.007	4.936
NGC1143	B	22.696	1.473	6.231	0.005	0.160	0.013	7.458
NGC1222*	A	26.367	0.807	6.223	0.002	0.153	0.006	3.244
NGC1365	A	32.675	1.013	6.216	0.002	0.169	0.007	3.541
NGC1566*	A	28.350	1.036	6.219	0.003	0.147	0.007	3.827
NGC1614*	A	62.998	2.944	6.229	0.003	0.141	0.008	2.908
NGC1667	A	22.479	2.130	6.226	0.008	0.177	0.021	10.439
NGC2146*	A	334.740	10.222	6.224	0.002	0.151	0.006	3.538
NGC2273	A	12.619	0.484	6.229	0.003	0.198	0.010	4.383
NGC2623*	A	18.147	0.518	6.222	0.002	0.138	0.005	3.274
NGC2992	B	21.411	1.301	6.234	0.005	0.192	0.015	6.077
NGC3079*	A	87.002	2.532	6.219	0.002	0.161	0.006	3.278
NGC3227*	A	24.795	1.318	6.218	0.004	0.167	0.011	4.418
NGC3256*	A	120.455	4.367	6.213	0.003	0.148	0.007	3.916
NGC3310*	A	39.139	1.175	6.222	0.002	0.161	0.006	3.374
NGC3511	B	25.836	1.976	6.238	0.008	0.224	0.020	5.848
NGC3556*	A	21.479	0.657	6.207	0.002	0.149	0.006	3.398
NGC3628*	A	75.757	2.304	6.218	0.002	0.143	0.005	2.679
NGC3786*	A	4.701	0.695	6.201	0.010	0.148	0.028	7.798
NGC3982	B	20.085	1.241	6.235	0.005	0.179	0.013	6.602
NGC4088*	A	13.764	0.410	6.215	0.002	0.145	0.005	2.587
NGC4194*	A	83.204	2.671	6.217	0.002	0.148	0.006	3.778
NGC4388	A	18.174	0.864	6.220	0.004	0.186	0.011	4.722
NGC4676*	A	11.294	0.465	6.219	0.003	0.141	0.007	3.152
NGC4818*	A	45.248	1.499	6.219	0.002	0.135	0.005	2.490
NGC4945*	A	111.908	9.806	6.223	0.005	0.116	0.012	7.312

Table A2 *– continued*

Source	Class	A (Jy sr^{-1})	Err A (Jy sr^{-1})	λ_c (μm)	Err λ_c (μm)	FWHM	Err FWHM	rms (%)
NGC5005	A	17.236	0.666	6.212	0.003	0.157	0.008	4.646
NGC5033	A	103.131	3.670	6.226	0.003	0.182	0.008	3.797
NGC5135	A	45.839	1.783	6.225	0.003	0.156	0.007	4.074
NGC5194	A	135.664	3.886	6.227	0.002	0.176	0.006	3.395
NGC5256*	A	18.107	0.654	6.216	0.002	0.138	0.006	3.635
NGC5674	A	1.939	0.036	6.219	0.002	0.256	0.006	1.332
NGC5953	B	13.449	0.467	6.239	0.003	0.165	0.007	4.183
NGC6810*	A	56.167	1.677	6.218	0.002	0.146	0.005	2.894
NGC6890*	A	11.585	0.861	6.225	0.005	0.173	0.017	6.735
NGC7130	B	18.447	0.331	6.244	0.001	0.171	0.004	2.149
NGC7252*	A	23.719	0.900	6.219	0.003	0.149	0.007	3.234
NGC7469*	A	58.434	2.659	6.220	0.003	0.143	0.008	4.315
NGC7496	A	13.969	0.896	6.212	0.005	0.169	0.013	8.060
NGC7582*	A	88.536	3.987	6.221	0.003	0.137	0.007	4.654
NGC7590*	A	14.060	1.157	6.220	0.005	0.154	0.017	6.391
NGC7603*	A	8.112	0.852	6.193	0.007	0.152	0.021	9.211
NGC7714*	A	28.309	1.152	6.222	0.003	0.138	0.006	2.478
SDSS_J005621.72+003235.8*	C	0.948	0.096	6.325	0.014	0.392	0.053	10.465
SJ103837.03+582214.8	A	0.222	0.026	6.193	0.011	0.216	0.033	12.454
SJ104217.17+575459.2	B	0.205	0.013	6.241	0.006	0.247	0.019	4.945
SJ104731.08+581016.1	A	0.251	0.022	6.215	0.007	0.185	0.021	8.785
SST172458.3+591545	B	0.115	0.008	6.233	0.005	0.160	0.014	7.053
SWIRE4_J103637.18+584217.0*	C	0.229	0.014	6.330	0.008	0.275	0.020	9.759
SWIRE4_J104057.84+565238.9	A	0.099	0.006	6.220	0.005	0.192	0.014	5.687
SWIRE4_J104117.93+595822.9	A	0.105	0.003	6.221	0.003	0.200	0.008	2.939
SWIRE4_J104830.58+591810.2*	A	0.208	0.008	6.213	0.003	0.164	0.009	4.055
SWIRE4_J105943.83+572524.9*	A	0.085	0.009	6.206	0.007	0.136	0.017	10.854
UGC5101*	A	14.196	0.681	6.213	0.003	0.150	0.009	5.359
UGC7064*	B	11.935	1.186	6.245	0.011	0.227	0.029	11.408
UGC12138	A	2.622	0.118	6.222	0.003	0.155	0.009	3.400

*Objects with profilesle's red tail disconsidered from the fit.

Table A3. Values of r_{PDR} and F_{25}/F_{20} ratio for sources from the MIR_SB sample (*Spitzer*/IRS ATLAS, version 1.0).

ID	r_{PDR}	Err r_{PDR}	F_{25}/F_{20}	Err F_{25}/F_{20}
3C293	0.201	0.002	1.273	0.016
3C31	0.277	0.002	1.017	0.019
AGN15	0.168	0.009	1.521	0.051
Arp220	0.268	0.001	3.89	0.009
CGCG381-051	0.329	0.013	1.088	0.022
E12-G21	0.328	0.008	1.162	0.035
EIRS-14	0.485	0.038	–	–
EIRS-2	0.556	0.019	–	–
EIRS-41	0.236	0.044	0.789	0.149
GN26	0.617	0.02	–	–
IC342	0.413	0.001	2.243	0.004
IRAS02021−2103	0.226	0.002	1.873	0.007
IRAS02480−3745	0.472	0.005	3.205	0.029
IRAS03209−0806	0.379	0.003	1.914	0.011
IRAS04074−2801	0.319	0.002	2.854	0.021
IRAS05020−2941	0.396	0.003	3.134	0.019
IRAS08591+5248	0.51	0.003	1.866	0.018
IRAS10594+3818	0.497	0.002	2.128	0.01
IRAS12447+3721	0.355	0.003	2.348	0.016
IRAS13106−0922	0.462	0.003	4.878	0.108
IRAS14121−0126	0.448	0.003	2.045	0.013
IRAS14197+0813	0.346	0.004	1.974	0.013
IRAS14202+2615	0.339	0.002	1.99	0.006
IRAS14485−2434	0.293	0.002	1.869	0.011
IRAS15043+5754	0.529	0.002	2.936	0.024
IRAS21477+0502	0.251	0.001	1.852	0.006

Table A3 – *continued*

ID	r_{PDR}	Err r_{PDR}	F_{25}/F_{20}	Err F_{25}/F_{20}
IRAS22088−1831	0.263	0.001	3.281	0.013
IRAS_00091−0738	0.25	0.003	2.961	0.015
IRAS_00456−2904	0.529	0.003	2.039	0.012
IRAS_01199−2307	0.3	0.003	2.537	0.016
IRAS_01355−1814	0.197	0.004	2.834	0.024
IRAS_01494−1845	0.458	0.006	2.009	0.023
IRAS_02411+0353	0.38	0.003	1.601	0.007
IRAS_03250+1606	0.45	0.003	2.056	0.019
IRAS_03521+0028	0.354	0.004	2.7	0.018
IRAS_08201+2801	0.343	0.004	2.214	0.012
IRAS_09039+0503	0.371	0.006	2.87	0.036
IRAS_09116+0334	0.529	0.004	1.758	0.019
IRAS_09463+8141	0.38	0.008	3.262	0.077
IRAS_09539+0857	0.304	0.004	3.438	0.035
IRAS_10190+1322	0.559	0.001	1.926	0.009
IRAS_10485−1447	0.19	0.003	2.572	0.02
IRAS_10494+4424	0.523	0.003	2.551	0.02
IRAS_11130−2659	0.279	0.004	3.119	0.029
IRAS_11387+4116	0.479	0.006	1.986	0.023
IRAS_11506+1331	0.287	0.048	2.274	0.011
IRAS_12112+0305	0.403	0.003	2.637	0.014
IRAS_12359−0725	0.168	0.004	2.238	0.013
IRAS_13335−2612	0.493	0.003	2.091	0.02
IRAS_13469+5833	0.346	0.006	2.535	0.012
IRAS_13509+0442	0.458	0.004	2.021	0.018
IRAS_13539+2920	0.522	0.003	2.274	0.018
IRAS_14060+2919	0.499	0.003	1.757	0.011
IRAS_14252−1550	0.39	0.005	2.212	0.028
IRAS_14348−1447	0.346	0.003	2.754	0.014
IRAS_15206+3342	0.239	0.003	1.457	0.005
IRAS_15225+2350	0.219	0.041	2.097	0.01
IRAS_16090−0139	0.291	0.002	2.336	0.011
IRAS_16300+1558	0.269	0.04	3.062	0.02
IRAS_16333+4630	0.41	0.004	2.124	0.018
IRAS_16474+3430	0.467	0.003	2.084	0.013
IRAS_16487+5447	0.354	0.003	2.83	0.02
IRAS_17028+5817	0.513	0.004	2.55	0.027
IRAS_17068+4027	0.294	0.003	2.013	0.01
IRAS_20414−1651	0.417	0.006	3.185	0.025
IRAS_21208−0519	0.468	0.004	2.041	0.02
IRAS_21329−2346	0.395	0.005	3.13	0.038
IRAS_22206−2715	0.405	0.006	3.139	0.038
IRAS_22491−1808	0.352	0.029	2.818	0.014
IRAS_23129+2548	0.342	0.003	2.766	0.014
IRAS_23234+0946	0.289	0.005	2.38	0.018
LH_H901A	0.217	0.011	–	–
M+0-29-23	0.526	0.009	1.332	0.023
M-2-40-4	0.164	0.004	1.029	0.014
M-5-13-17	0.237	0.009	1.054	0.021
MIPS15755	0.373	0.026	–	–
MIPS180	0.057	0.044	–	–
MIPS22307	0.286	0.032	–	–
MIPS22352	0.534	0.041	–	–
MIPS562	0.553	0.054	–	–
MIPS8040	0.293	0.031	–	–
Mrk1066	0.291	0.002	1.489	0.004
Mrk273	0.22	0.002	2.491	0.008
Mrk334	0.326	0.002	1.361	0.004
Mrk471	0.427	0.005	1.224	0.014
Mrk52	0.318	0.005	1.142	0.005
Mrk609	0.47	0.003	1.33	0.008
Mrk622	0.199	0.004	1.325	0.006

Table A3 – *continued*

ID	r_{PDR}	Err r_{PDR}	F_{25}/F_{20}	Err F_{25}/F_{20}
Mrk883	0.247	0.004	1.396	0.008
Mrk938	0.498	0.005	1.834	0.019
Murphy22	0.423	0.025	–	–
Murphy3	0.382	0.025	–	–
Murphy8	0.391	0.038	–	–
NGC1056	0.662	0.007	1.394	0.037
NGC1097	0.572	0.001	1.274	0.004
NGC1125	0.303	0.061	1.368	0.022
NGC1143	0.49	0.009	–	–
NGC1222	0.436	0.002	1.461	0.005
NGC1365	0.173	0.001	1.562	0.003
NGC1566	0.422	0.003	1.053	0.005
NGC1614	0.399	0.001	1.288	0.003
NGC1667	0.626	0.009	1.304	0.045
NGC2146	0.656	0.012	2.007	0.003
NGC2273	0.23	0.001	1.206	0.004
NGC2623	0.442	0.002	2.585	0.011
NGC2992	0.21	0.005	1.053	0.012
NGC3079	0.651	0.043	2.312	0.011
NGC3227	0.172	0.002	1.067	0.004
NGC3256	0.414	0.001	1.735	0.002
NGC3310	0.557	0.002	1.62	0.007
NGC3511	0.701	0.013	1.242	0.062
NGC3556	0.607	0.003	1.881	0.014
NGC3628	0.656	0.029	2.311	0.009
NGC3786	0.288	0.003	1.241	0.008
NGC3982	0.568	0.009	1.18	0.028
NGC4088	0.539	0.004	1.542	0.012
NGC4194	0.477	0.001	1.634	0.004
NGC4388	0.196	0.004	1.301	0.011
NGC4676	0.635	0.003	1.706	0.01
NGC4818	0.355	0.001	1.298	0.003
NGC4945	0.598	0.001	4.55	0.01
NGC5005	0.457	0.007	1.514	0.033
NGC5033	0.562	0.002	1.162	0.005
NGC5135	0.477	0.004	1.376	0.012
NGC513	0.465	0.014	1.046	0.037
NGC5194	0.588	0.001	1.26	0.004
NGC520	0.619	0.01	2.521	0.007
NGC5256	0.54	0.008	1.602	0.028
NGC5674	0.21	0.005	–	–
NGC5953	0.556	0.008	1.485	0.019
NGC660	0.558	0.026	1.934	0.004
NGC6810	0.458	0.004	1.092	0.008
NGC6890	0.285	0.008	1.041	0.02
NGC7130	0.267	0.005	1.44	0.009
NGC7252	0.678	0.002	1.564	0.009
NGC7469	0.292	0.003	1.181	0.006
NGC7496	0.288	0.005	1.499	0.012
NGC7582	0.405	0.002	1.451	0.008
NGC7590	0.623	0.011	1.206	0.055
NGC7603	0.158	0.003	0.83	0.02
NGC7714	0.359	0.002	1.361	0.004
SDSS_J005621.72+003235.8	0.174	0.005	–	–
SJ103837.03+582214.8	0.373	0.063	–	–
SJ104217.17+575459.2	0.574	0.124	–	–
SJ104731.08+581016.1	0.21	0.042	–	–
SST172458.3+591545	0.215	0.021	–	–
SWIRE4_J103637.18+584217.0	0.205	0.015	–	–
SWIRE4_J104117.93+595822.9	0.333	0.045	–	–
SWIRE4_J105943.83+572524.9	0.295	0.026	–	–
UGC12138	0.154	0.002	1.119	0.005
UGC5101	0.325	0.003	1.824	0.006
UGC7064	0.345	0.012	0.966	0.027

APPENDIX B: COMPARISON OF THE 6.2 μm RESULTS FOR THE CONTINUUM DECOMPOSITION

The Tables B1–B3 and the Figs B1–B3 compare the differences among the 6.2 μm band fits according to the spectral continuum contribution fitted with the three methods described below. Such contribution was subtracted from the spectra before the band was fitted. 20 galaxies were selected for this comparison, 10 with strong PAH plateaus, and 10 with weak or none plateaus (see Section 3). To standardize the comparison, in all cases the band was fitted using the same method. We fitted using only one Gaussian profile and the submodule *curve_fit*. The following methodology was applied.

(i) Subtraction of the continuum and ionic and molecular contributions fitted with PAHFIT,

(ii) only the subtraction of the continuum contribution fitted with PAHFIT, and

(iii) subtraction of the ionic and molecular contributions fitted with PAHFIT and the subtraction of the continuum contribution decomposed with spline.

The central wavelengths, which are the objective of this work, presented values range within the uncertainty bar of the parameter. Therefore, the method chosen does not influence the final results in our analysis. On the other hand, the band intensity and the FWHM

Table B1. Results of the fitted amplitude (A) of the band of 6.2 μm for each continuum decomposition method.

ID	Plateau	(i) A (Jy sr^{-1})	(ii) A (Jy sr^{-1})	(iii) A (Jy sr^{-1})
3C31	yes	2.422 ± 0.078	2.422 ± 0.078	1.611 ± 0.043
IRAS_00456−2904	yes	8.190 ± 0.532	8.190 ± 0.532	5.286 ± 0.224
IRAS_09116+0334	yes	4.386 ± 0.215	4.386 ± 0.215	2.959 ± 0.127
IRAS_10190+1322	yes	15.824 ± 0.710	15.824 ± 0.710	11.248 ± 0.452
IRAS_16474+3430	yes	7.327 ± 0.449	7.327 ± 0.449	4.680 ± 0.169
IRAS08591+5248	yes	3.620 ± 0.201	3.945 ± 0.213	2.224 ± 0.098
IRAS14202+2615	yes	7.619 ± 0.272	7.619 ± 0.272	5.443 ± 0.188
IRAS15043+5754	yes	4.105 ± 0.207	4.105 ± 0.207	2.390 ± 0.066
Mrk1066	no	35.947 ± 0.476	37.757 ± 0.762	19.651 ± 0.593
Mrk334	no	26.897 ± 2.344	26.897 ± 2.344	16.966 ± 0.760
Mrk52	no	15.240 ± 0.640	15.240 ± 0.640	12.490 ± 0.481
Mrk609	no	15.649 ± 0.807	15.649 ± 0.807	10.671 ± 0.479
Mrk622	no	3.440 ± 0.331	3.945 ± 0.199	2.439 ± 0.479
Mrk883	no	2.994 ± 0.089	2.994 ± 0.089	2.445 ± 0.061
NGC1097	yes	191.185 ± 8.974	193.840 ± 7.407	117.594 ± 5.763
NGC1222	no	39.608 ± 1.380	39.608 ± 1.380	26.367 ± 0.807
NGC1365	no	40.451 ± 1.171	40.451 ± 1.171	32.675 ± 1.013
NGC2273	no	22.736 ± 0.326	23.609 ± 0.496	12.619 ± 0.484
NGC2992	no	30.599 ± 1.694	30.599 ± 1.694	21.411 ± 1.301
NGC3556	yes	35.212 ± 1.338	35.212 ± 1.338	21.479 ± 0.657

Table B2. Results of the fitted central wavelength (λ_c) of the band of 6.2 μm for each continuum decomposition method.

ID	Plateau	(i) λ_c (μm)	(ii) λ_c (μm)	(iii) λ_c (μm)
3C31	yes	6.233 ± 0.003	6.233 ± 0.003	6.230 ± 0.002
IRAS_00456−2904	yes	6.238 ± 0.007	6.238 ± 0.007	6.229 ± 0.003
IRAS_09116+0334	yes	6.231 ± 0.005	6.231 ± 0.005	6.228 ± 0.003
IRAS_10190+1322	yes	6.233 ± 0.005	6.233 ± 0.005	6.225 ± 0.003
IRAS_16474+3430	yes	6.251 ± 0.006	6.251 ± 0.006	6.245 ± 0.002
IRAS08591+5248	yes	6.216 ± 0.005	6.203 ± 0.004	6.210 ± 0.003
IRAS14202+2615	yes	6.212 ± 0.003	6.212 ± 0.003	6.210 ± 0.002
IRAS15043+5754	yes	6.214 ± 0.005	6.214 ± 0.005	6.205 ± 0.002
Mrk1066	no	6.231 ± 0.001	6.230 ± 0.002	6.227 ± 0.003
Mrk334	no	6.245 ± 0.009	6.245 ± 0.009	6.244 ± 0.004
Mrk52	no	6.214 ± 0.003	6.214 ± 0.003	6.209 ± 0.003
Mrk609	no	6.225 ± 0.005	6.225 ± 0.005	6.225 ± 0.004
Mrk622	no	6.209 ± 0.008	6.197 ± 0.004	6.210 ± 0.007
Mrk883	no	6.229 ± 0.003	6.229 ± 0.003	6.231 ± 0.002
NGC1097	yes	6.217 ± 0.004	6.213 ± 0.003	6.214 ± 0.004
NGC1222	no	6.227 ± 0.003	6.227 ± 0.003	6.223 ± 0.002
NGC1365	no	6.216 ± 0.002	6.216 ± 0.002	6.216 ± 0.002
NGC2273	no	6.232 ± 0.001	6.232 ± 0.001	6.229 ± 0.003
NGC2992	no	6.237 ± 0.005	6.237 ± 0.005	6.234 ± 0.005
NGC3556	yes	6.213 ± 0.003	6.213 ± 0.003	6.207 ± 0.002

Table B3. Results of the fitted FWHM of the band of 6.2 μm for each continuum decomposition method.

ID	Plateau	(i) FWHM	(ii) FWHM	(iii) FWHM
3C31	yes	0.233 ± 0.010	0.233 ± 0.010	0.197 ± 0.007
IRAS_00456−2904	yes	0.186 ± 0.016	0.186 ± 0.016	0.132 ± 0.008
IRAS_09116+0334	yes	0.202 ± 0.014	0.202 ± 0.014	0.162 ± 0.009
IRAS_10190+1322	yes	0.201 ± 0.011	0.201 ± 0.011	0.162 ± 0.008
IRAS_16474+3430	yes	0.192 ± 0.014	0.195 ± 0.014	0.143 ± 0.006
IRAS08591+5248	yes	0.178 ± 0.008	0.181 ± 0.013	0.144 ± 0.008
IRAS14202+2615	yes	0.196 ± 0.013	0.178 ± 0.008	0.151 ± 0.006
IRAS15043+5754	yes	0.195 ± 0.014	0.196 ± 0.013	0.134 ± 0.005
Mrk1066	no	0.269 ± 0.004	0.286 ± 0.007	0.205 ± 0.008
Mrk334	no	0.209 ± 0.024	0.209 ± 0.024	0.156 ± 0.009
Mrk52	no	0.168 ± 0.009	0.168 ± 0.009	0.146 ± 0.007
Mrk609	no	0.203 ± 0.013	0.203 ± 0.013	0.164 ± 0.009
Mrk622	no	0.170 ± 0.022	0.184 ± 0.013	0.141 ± 0.016
Mrk883	no	0.196 ± 0.007	0.196 ± 0.007	0.174 ± 0.005
NGC1097	yes	0.212 ± 0.013	0.207 ± 0.010	0.163 ± 0.010
NGC1222	no	0.195 ± 0.009	0.195 ± 0.009	0.153 ± 0.006
NGC1365	no	0.186 ± 0.007	0.186 ± 0.007	0.169 ± 0.007
NGC2273	no	0.262 ± 0.005	0.275 ± 0.007	0.198 ± 0.010
NGC2992	no	0.223 ± 0.015	0.223 ± 0.015	0.192 ± 0.015
NGC3556	yes	0.198 ± 0.010	0.198 ± 0.010	0.149 ± 0.006

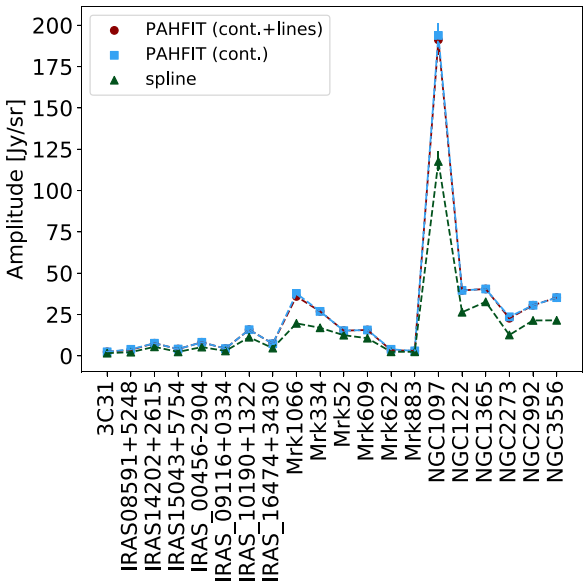

Figure B1. Results for the 6.2 μm profile amplitude depending on each decomposition method – (i) circle; (ii) square; and (iii) triangle.

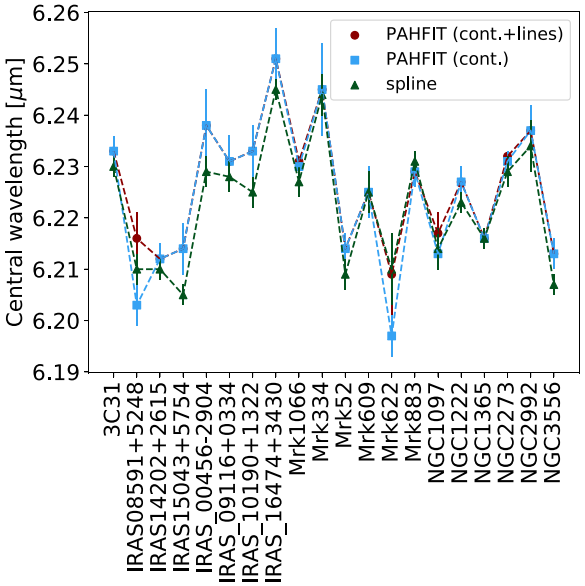

Figure B2. Results for the 6.2 μm profile central wavelength depending on each decomposition method – (i) circle; (ii) square; and (iii) triangle.

even doubled their values depending on whether the fit of the continuum was performed by PAHFIT or by the spline.

The methods (i) and (ii) resulted, in general, in the same values. The only difference between both is whether the ionic and molecular lines contributions were subtracted or not from the spectra before the band analysis. As no large blending of these lines is known, this similarity in the results was already expected, revealing that the contribution of these lines is insignificant for the final results.

Therefore, the greatest discrepancy is due to the program used. To better understand the results, the spline decomposition is preferable to the PAHFIT fit for our particular analysis because it already considers the PAH plateau of 5–10 μm rather than diluting it in the Drude profiles of the PAH bands (Peeters et al. 2017). Moreover, this difference in the band intensity is crucial when considering other PAH bands such as the 7.7 μm band, for instance.

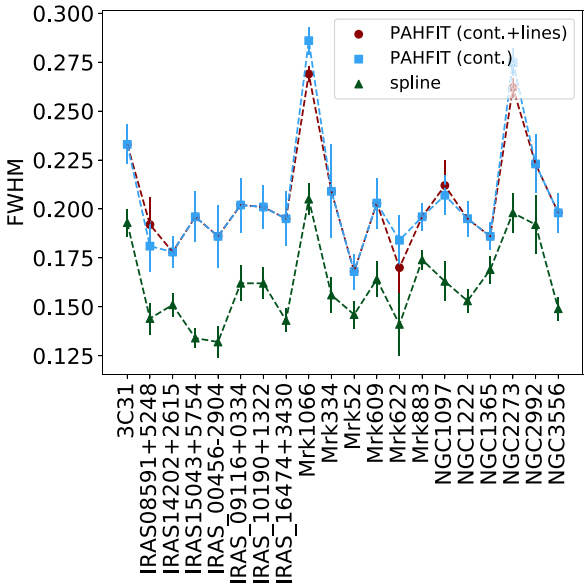

Figure B3. Results for the 6.2 μm profile FWHM depending on each decomposition method – (i) circle; (ii) square; and (iii) triangle.

This paper has been typeset from a TEX/LATEX file prepared by the author.